Journal of Nanobiotechnology

RESEARCH

Open Access

Tumor microenvironment-responsive manganese-based nano-modulator activate the cGAS-STING pathway to enhance innate immune system response

Xiayi Liang[1†], Duo Wang[2†], Yuanquan Zhao[3†], Xiaobo Wang[1], Siyang Yao[3], Wei Huang[3], Yongyu Yang[3], Xiaofeng Dong[3*], Lei Zhang[2*] and Jianrong Yang[3*]

Abstract

Background Manganese ions (Mn^{2+}) combined with adjuvants capable of damaging and lysing tumor cells form an antitumor nano-modulator that enhances the immune efficacy of cancer therapy through the cascade activation of the cyclic GMP-AMP interferon gene synthase-stimulator (cGAS-STING) pathway, which underscores the importance of developing antitumor nano-modulators, which induce DNA damage and augment cGAS-STING activity, as a critical future research direction.

Methods and Results We have successfully synthesized an antitumor nano-modulator, which exhibits good dispersibility and biosafety. This nano-modulator is engineered by loading manganese dioxide nanosheets (M-NS) with zebularine (Zeb), known for its immunogenicity-enhancing effects, and conducting targeted surface modification using hyaluronic acid (HA). After systemic circulation to the tumor site, Mn^{2+}, Zeb, and reactive oxygen species (ROS) are catalytically released in the tumor microenvironment by H^+ and H_2O_2. These components can directly or indirectly damage the DNA or mitochondria of tumor cells, thereby inducing programmed cell death. Furthermore, they promote the accumulation of double-stranded DNA (dsDNA) in the cytoplasm, enhancing the activation of the cGAS-STING signalling pathway and boosting the production of type I interferon and the secretion of pro-inflammatory cytokines. Additionally, Zeb@MH-NS enhances the maturation of dendritic cells, the infiltration of cytotoxic T lymphocytes, and the recruitment of natural killer cells at the tumor site.

Conclusions This HA-modified manganese-based hybrid nano-regulator can enhance antitumor therapy by boosting innate immune activity and may provide new directions for immunotherapy and clinical translation in cancer.

Keywords Tumor microenvironment, Innate immunity, cGAS-STING pathway, Manganese immunotherapy

†Xiayi Liang, Duo Wang and Yuanquan Zhao have authors contributed equally to this work.

*Correspondence:
Xiaofeng Dong
gandanyingcai@163.com
Lei Zhang
zhang_lei@seu.edu.cn
Jianrong Yang
gandansurgery2014@163.com
Full list of author information is available at the end of the article

Graphical Abstract

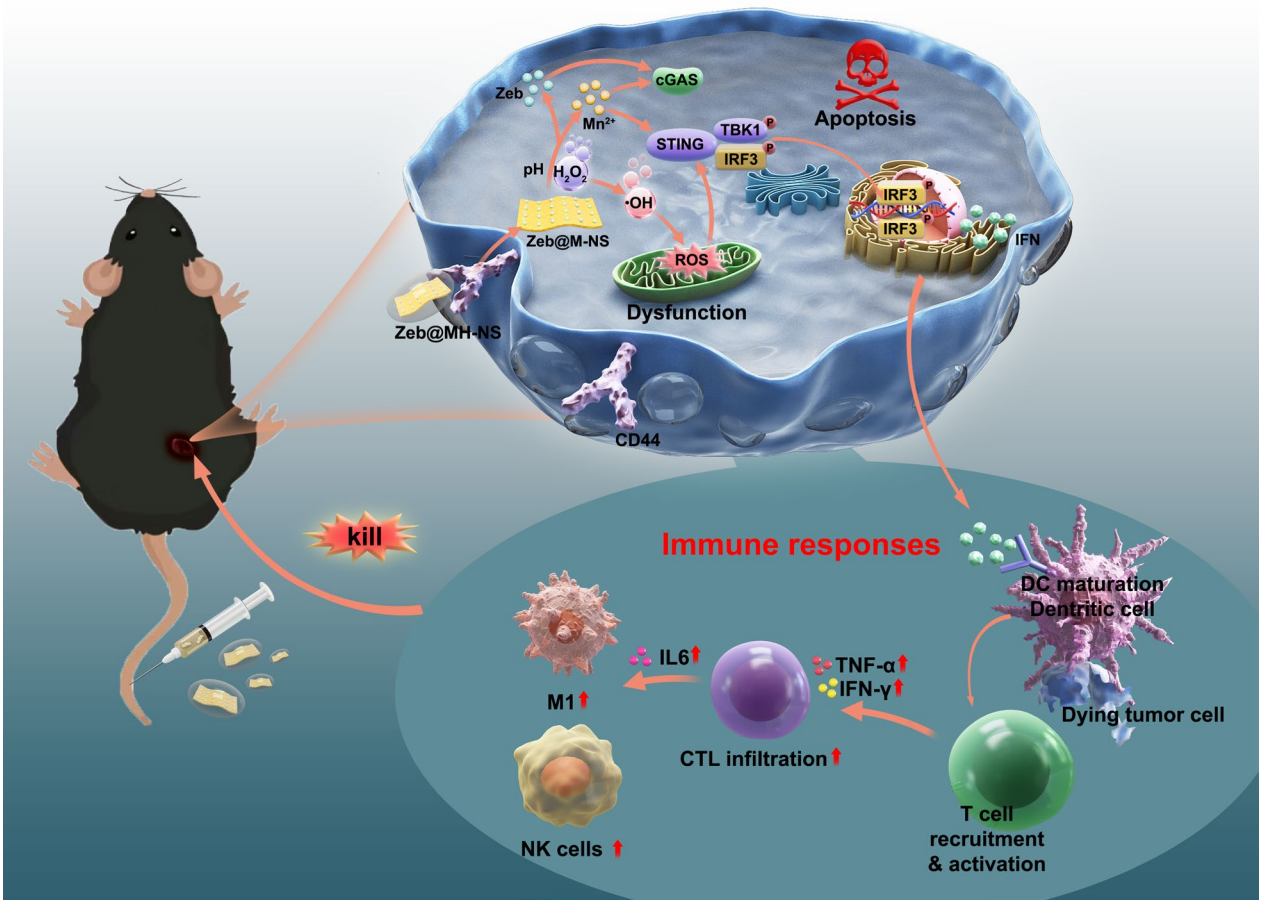

Introduction

Natural immunity constitutes the body's primary defence mechanism against pathogens and tumor cells by conferring resistance and facilitating antigen presentation [1, 2]. For most patients whose tumors are inoperable or who have undergone surgical resection, activating the adaptive immune response through pharmacological means can potentially control cancer progression promptly. However, current clinical immunotherapy strategies have not yet achieved optimal antitumor effects, highlighting the need for innovative approaches to activate innate immunity and enhance the efficacy of cancer immunotherapy [3–5]. Cyclic GMP-AMP synthase (cGAS) plays a pivotal role in detecting microbial DNA invasions and monitoring cellular stress responses and genomic stability, which is crucial in autoimmune diseases, cellular damage, aging, immune surveillance, and treatment of tumors. Antitumor drugs induce the accumulation of free double-stranded DNA (dsDNA) in the cytoplasm by damaging DNA within cancer cells. The cGAS detects dsDNA and generates the second messenger molecule, 2′3′-cGAMP, which activates the STING pathway, producing interferon-stimulated genes. This process results in the phosphorylation of downstream junction proteins, catalyzing a potent immune response characterized by the release of type I interferons (IFNs) and inflammatory cytokines, effectively mobilizing immune cells and maximizing the innate immune defence [6–9].

Manganese (Mn) is instrumental in activating the innate immune response and tumor immune surveillance [7, 10, 11]. Mn^{2+} enhances the sensitivity of cGAS to DNA by 10,000-fold, robustly activating the intracellular cGAS-STING pathway and exerting a potent antiviral capacity [7]. Under physiological conditions, intracellularly released Mn^{2+} also activates the cGAS-STING pathway in a dsDNA-dependent/independent manner, enhancing the catalytic efficiency of cGAS. Mn^{2+} deficiency remarkably increases cancer incidence,

confirming Mn^{2+} as a secondary cGAS activator in the cells. The manganese-based nanoadjuvant acts as a mucosal immune adjuvant by inducing the formation of secretory IgA, boosting T cells' ability to create large quantities of antibodies, and stimulating mucosal immunological responses [12, 13]; this predicts that manganese immunotherapy has excellent potential for clinical application. Consequently, numerous studies have investigated antitumor nano-modulator based on Mn^{2+} and nanocatalytic medicine, demonstrating immune-sensitizing efficacy in animal models and early clinical trials [14–16]. The anticancer nano-modulator incorporating MnO_2 with the PI3Kγ blocker IPI549, upon activation in the local tumor environment, degrades and releases Mn^{2+}, oxygen molecules (O_2), and IPI549, moderating the hypoxic conditions of the tumor and reducing PD-L1 immunosuppressive molecules on the cell surface [14]. The nano-modulators promote MDSC activity, drive the polarization of tumor-associated macrophages (TAMs) toward the M1 phenotype, reactivate killer T cells, and curb the spread of cancer cells. Previous studies showed that combined manganese dioxide and IPI549 to create a radiotherapy-sensitizing antitumor nano-modulator targeting myeloid cells to reshape the postoperative tumor microenvironment (TME). This strategy catalyzes the conversion of endogenous H_2O_2 into O_2, mitigating hypoxia, enhancing the immunogenic effect of the immunosuppressive microenvironment, and enhancing susceptibility to anti-PD-L1 therapy, thus stimulating a robust immune memory effect to resist tumor recurrence [15].

Furthermore, leveraging the Fenton-like catalytic and immunogenic cell death-inducing activities of MnO_2 nanosheets (M-NS), some academics developed a hydrogel encapsulating M-NS and the vascular destructor CA4P to intensify tumor-starvation therapy and enhance immunotherapy. In the tumor microenvironment, M-NS catalyzes hydrogen peroxide to generate O_2, alleviating tumor hypoxia induced by vascular disrupting agents; it also decomposes into water-soluble and non-toxic Mn^{2+} to avoid toxicity. M-NS can increase oxidative damage in the tumor by depleting glutathione, H_2O_2, and H^+[16]. Therefore, under conditions of tumor cell starvation caused by vascular disruptor CA4P treatment, M-NS has the potential to reverse the tumor immune microenvironment and enhance antitumor immunity to eradicate occult microdamage at the peripheral margins. M-NS, both as a standalone agent and as a drug carrier, enhances the immunoreactivity of cancer cell neoantigens, triggers effective immune responses, and reshapes the immune status of the tumor microenvironment, thus pioneering a new pathway for localized and regional tumor immunotherapy.

Zeb, a potent inhibitor of DNA methyltransferases, effectively enhances the immune properties of tumor cells by disrupting their DNA methylation processes, thus increasing their susceptibility to detection and elimination by the immune system [17–21]. Research has demonstrated that Zeb augments the sensitivity of cancer cells to the cGAS-STING pathway, facilitates intracellular DNA accumulation, and promotes the production of DNA-triggered interferon, significantly improving the visibility of cancer cells to the immune system. This activity not only counters the immune suppression commonly observed in the tumor microenvironment but also bolsters the body's capacity to eradicate cancer cells [22–24]. In light of these findings, we explored the synergistic effects of the immunomodulatory mechanisms of Zeb combined with Mn^{2+} in cancer therapy.

First, Zeb was packed into a novel nano-modulator, and we used M-NS as a carrier. Afterwards, we surface-modified Zeb@MH-NS, a unique cancer-fighting nano-activator that is capable of targeting the tumor cells' CD44 receptor, by employing HA, Zeb, ROS, and Mn^{2+} can develop in weakly acidic environments with the help of hydrogen peroxide. Through direct or indirect interactions with tumor cells or their internal mitochondria, these substances contribute to the build-up of double-stranded DNA (dsDNA) within the cell, aggravating the physiological consequences mediated by the cGAS-STING signalling pathway. Zeb@MH-NS also positively affected natural killer cell clustering around the tumor, cytotoxic T lymphocyte infiltration, and dendritic cell maturation. Furthermore, Zeb@MH-NS markedly increased the release of cytokines linked to inflammation and the synthesis of type I interferon (Scheme 1), promotes ICD, activates the immune system, and promotes the infiltration of CD8 T cells, NK cells, and M1-type macrophages in the tumor. Consequently, the engineered HA-modified manganese-based hybrid nano-activator presented in this research has the potential to amplify anticancer treatments through the augmentation of the body's inherent immune response, presenting a novel avenue for immunotherapeutic strategies and their clinical implementation in oncology.

Results and discussion

Synthesis characterization and performance testing of Zeb@MH-NS nanoparticles.

To synthesize a novel immunostimulatory antitumor nano-modulator, M-NS were prepared using a conventional method enhanced by ultrasonic treatment [25, 26]. The process involved oxidizing $MnCl_2$ with H_2O_2, exfoliating it with methylammonium hydroxide, and preparing a 200 nm flake morphology through ultrasonic treatment (Fig. 1A). To further validate the successful

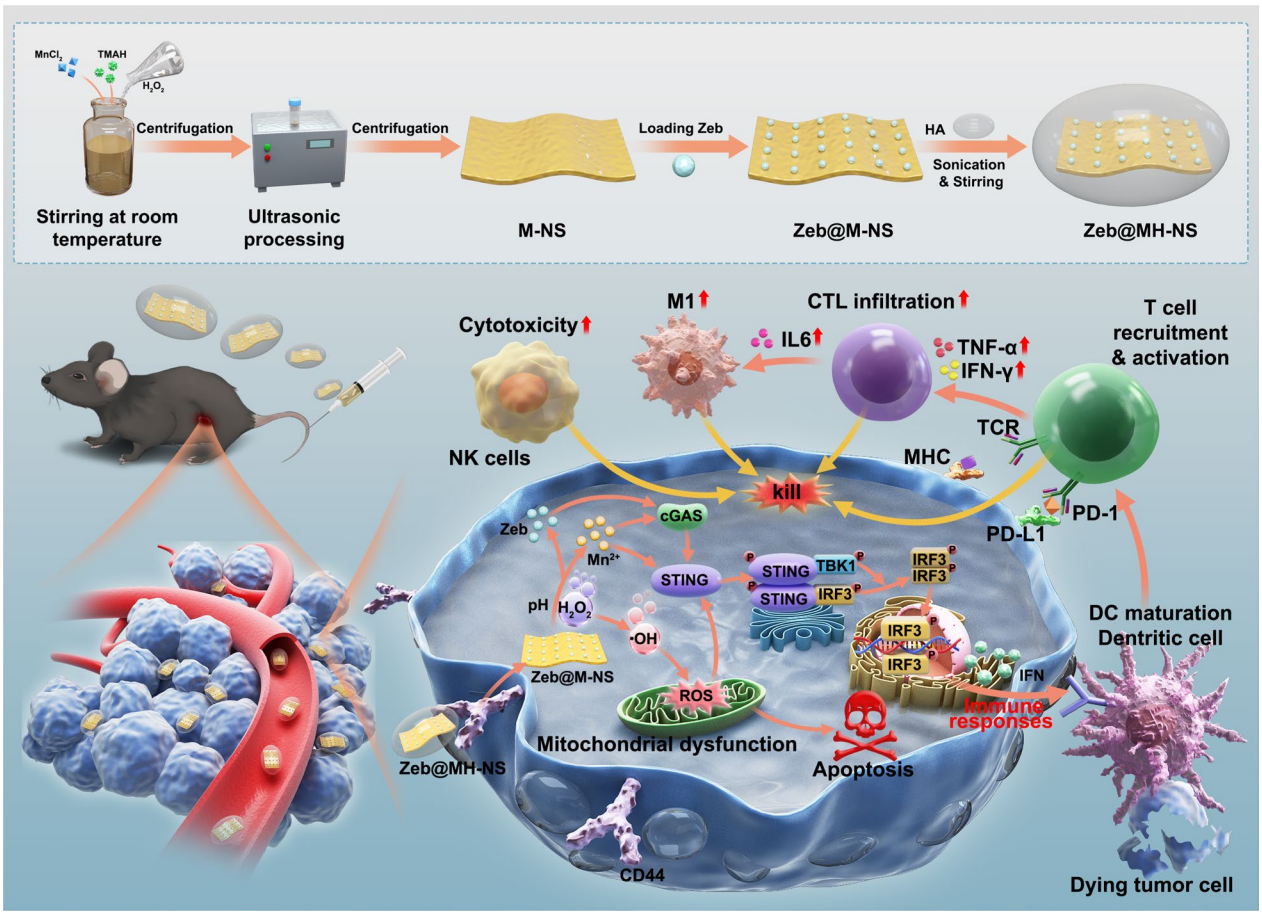

Scheme 1 Manganese-based natural immune nano-activators produce potent antitumor effects by enhancing the cGAS-STING pathway. M1, M1-like macrophage; DC, dendritic cell; CTL, cytotoxic T lymphocyte. NK cells, natural killer cells

preparation of M-NS, the distribution behaviours of Mn and O elements were directly shown by SEM (Fig. S1), STEM spectroscopic imaging (Fig. S2), and energy spectral surface scanning (Fig. S3). Subsequently, to verify the surface chemistry, species, and chemical valence states of the synthesized M-NS constituents and to determine their nanocatalysis efficacy, as shown in Fig. 1B, the characteristic splitting peaks of XPS showed Mn $2p_{3/2}$ and Mn $2p_{1/2}$ binding energies centred at 641.95 eV and 653.65 eV, and the predominant oxidation state of manganese was indicated as + 4 by the magnitude of the peaks' splitting, which means that the synthesized nanosheets have a nanocatalysis role in the oxidative reduction of tumor-enriched expressed H_2O_2 to hydroxyl radicals (• OH) with a killing effect [27]. The O elemental XPS signal centred at ~ 529.64 eV is shown in Fig. 1C. The results show similar binding energies to previous studies of manganese and oxygen elements within M-NS [28], suggesting that we successfully constructed a well-sized M-NS. Subsequently, we first determined the ultraviolet–visible spectroscopy (UV–Vis) of different concentrations of Zeb drug dissolved in PBS. We produced standard curves, which confirmed the characteristic absorption peak at 307 nm (Fig. S4). The optimal feeding ratio 1:1 for M-NS/Zeb was achieved, resulting in a superior loading capacity of approximately 46%, considering full drug utilization (Fig. S5).

Building on the previous work involving the surface modification of nanosheets with HA, which targets CD44 receptors on tumor cell membranes, the targeted delivery of anticancer drugs can be significantly facilitated [29–32]. This study employed HA to modify the surface of Zebularine-loaded manganese dioxide nanosheets (Zeb@M-NS). Upon TEM observation, it was found that the synthesized Zeb@MH-NS showed monolithic shape and good dispersion (Fig. 1D). Under energy spectroscopy, the three elements Mn, O, and N were uniformly distributed on the nanosheets (Fig. 1E). To verify the size and thickness of the synthesized nanosheets, the thickness of the synthesized nanosheets was verified to be about 3 nm by Atomic Force Microscopy (AFM) (Fig. 1F), and Malvern Zeta particle size found the particle size was

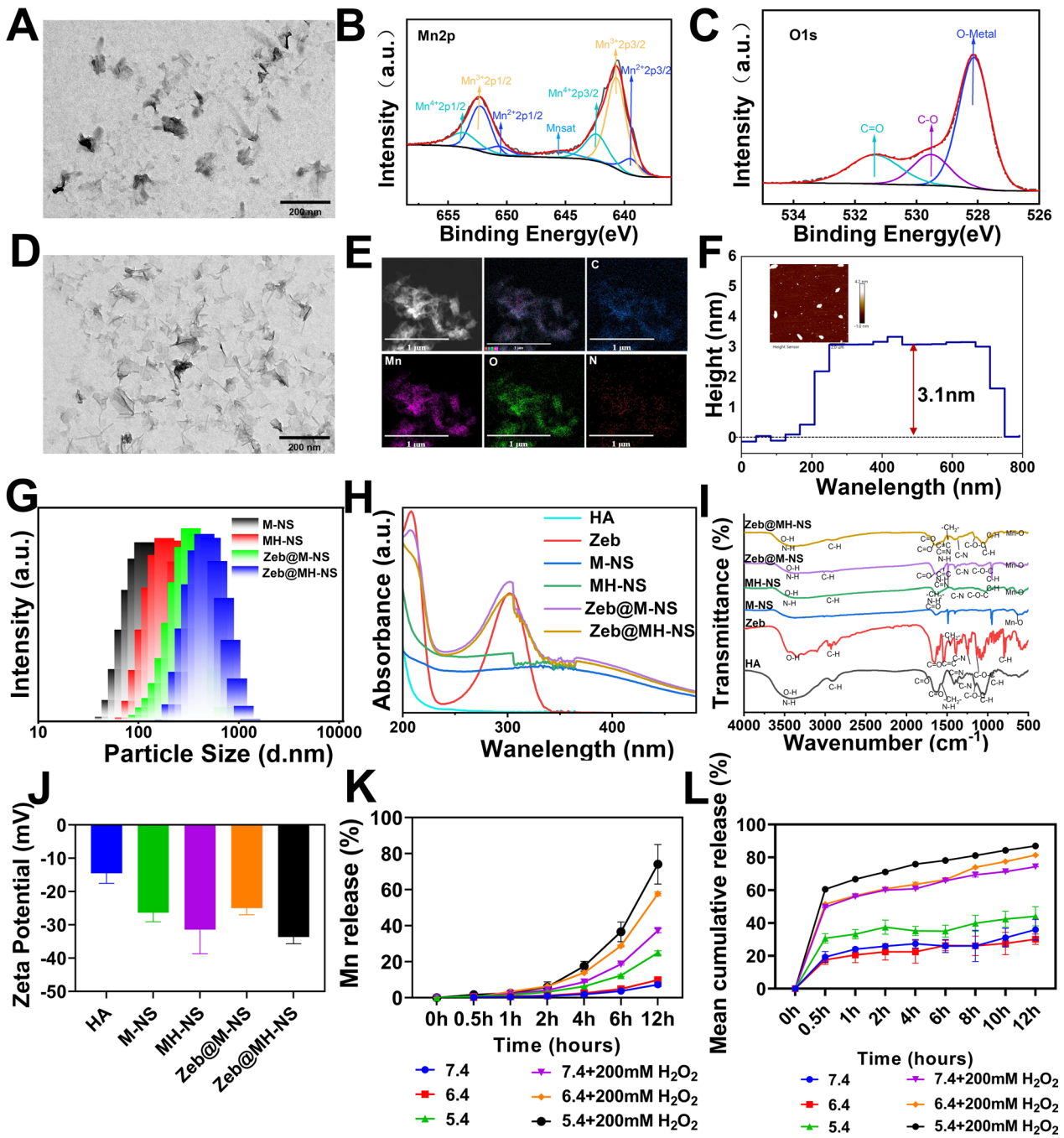

Fig. 1 Synthesis and characterization of Zeb@MH-NS nanoparticles. (A) TEM image of M-NS. (B) XPS spectrum of Mn 2p region. (C) XPS spectrum of O 1 s region. (D) T.E.M. of Zeb@MH-NS. (E) Elemental mapping of Mn, C, O, and N of Zeb@MH-NS. (F) Thickness distribution of the nanosheets of Zeb@MH-NS as measured by AFM Inset: AFM images of Zeb@MH-NS nanosheets. (G) Size distribution of M-NS, MH-NS, Zeb@M-NS, Zeb@MH-NS. (H) UV–vis of HA, Zeb, M-NS, MH-NS, Zeb@M-NS. (I) FTIR spectra of HA, Zeb, M-NS, MH-NS, Zeb@M-NS, Zeb@MH-NS. (J)Zeta potential of HA, M-NS, MH-NS, Zeb@M-NS, Zeb@MH-NS. (K) $Mn.^{2+}$ release profiles at pH 5.4, 6.4, and 7.4 with/without H_2O_2. (L) Drug release profiles at pH 5.4, 6.4, and 7.4 with/without H_2O_2

maintained in the range of 230–267 nm during HA and drug loading process (Fig. 1G). To understand the nature of Zeb@MH-NS, the UV–Vis of different subgroups showed characteristic absorption peaks at 307 nm and 200 nm in Zeb@MH-NS (Fig. 1H).

The absorption spectra of various components, including the Mn–O stretching vibration absorption peaks at

627 cm^{-1}, were examined via Fourier Transform Infrared Spectroscopy (FTIR) in the Zeb@MH-NS sample. The peak observed at a wavenumber of 1739 cm^{-1} corresponds to the C = O bond's stretching vibrational mode in the carboxylic group attached to HA. Meanwhile, the 1045 cm^{-1} and 946 cm^{-1} peaks represent the in-plane bending vibrations of the C-H bonds found in Zeb/HA. The peak at 1546 cm^{-1} can also be attributed to the bending vibration of the amide II band's N–H bond on HA and the stretching vibrations of the C = C and C = N bonds on Zeb. Lastly, the absorption peak observed at 1489 cm^{-1} is the -CH2 bending vibration absorption peak of Zeb/HA.

Moreover, as shown in Fig. 1I, Zeb@MH-NS has similar absorption peaks of Zeb and HA, which suggests that M-NS was successfully loaded with Zeb through electrostatic interactions and HA was successfully attached to the surface of M-NS nanosheets. X-ray diffraction (XRD) showed that M-NS had characteristic XRD absorption peaks ($2\theta \approx 37°$ and 65.36°). After HA surface modification, the characteristic XRD peaks of HA ($2\theta \approx 12.8°$ and 24.54°) were included in MH-NS (Fig. S6). The potentials of HA and M-NS were negative, and the potential values of HA-modified manganese dioxide nanosheets became larger (Fig. 1J), which indicated that HA successfully surface-modified the nanosheets. Based on the principle of charge homogeneity and repulsion, Zeb@MH-NS had good dispersion.

Several studies have demonstrated that M-NS nanopreparations are well stabilized in a neutral environment (pH = 7.4) but are susceptible to decomposition into Mn^{2+} ions by the weakly acidic pH and high H_2O_2 in the tumor microenvironment, which exerts the corresponding antitumor efficacy [33–35]. This study investigated the release dynamics of Zebularine (Zeb) and Mn^{2+} ions from the Zeb@MH-NS nanocarrier under simulated TME conditions. The nanocarrier was exposed to various acidic media (pH 5.4, 6.4, 7.4) with added hydrogen peroxide, employing a dialysis bag technique to monitor the in vitro release of these compounds [36, 37]. The removed liquid was examined using UV–Vis and inductively coupled plasma (ICP) to assess the drug and manganese ion release rates, respectively (Fig. 1K, L). The results indicated that Zeb@MH-NS exhibited effective cumulative release kinetics in acidic and H_2O_2-rich solutions, facilitating a faster and more pronounced release of the drug and manganese ions. It remained stable in the first two media: phosphate-buffered saline (PBS, pH = 7.4), Dulbecco's Modified Eagle Medium (DMEM) containing 10% fetal bovine serum (FBS) and deionized water (Fig. S7A). The particle size showed minimal variation (Fig. S7B), mirroring findings from other studies that investigated the responsiveness of manganese dioxide nanosheets to TME-induced degradation and controlled release mechanism [38–40], These results underscore the potential of Zeb@MH-NS for innovative applications in antitumor therapy.

Evaluation of Zeb@MH-NS targeting and ROS generation capacity

Research has highlighted that many cancer cell membranes, including those of HepG2, a human liver cancer cell line, exhibit CD44 receptors, facilitating the selective uptake of HA-complexed nanostructures such as the anticancer compound geraniol [41, 42]. The study utilized HepG2 cells as a control to evaluate the expression of CD44 receptors in Hepa1-6 cells. Using flow cytometry (FCM) with CD44-specific staining reagents (Fig. 2A), it was found that Hepa1-6 cells also expressed abundant CD44 receptors on their membranes (Fig. S8A), which implies that surface modification of this M-NS preparation with HA not only promotes the efficacy of having good dispersion but also targets Hepa1-6 cancer cells. Hepa1-6 cells were co-incubated with FITC-labeled Zeb@MH-NS and Zeb@M-NS (Fig. 2B, C, and S9). The cellular uptake of FITC-labeled Zeb@MH-NS by Hepa1-6 cells was monitored at various intervals using confocal laser-scanning microscopy (CLSM) and FCM, both of which showed an incremental increase in green fluorescence compared to Zeb@M-NS (Fig. S9C).

Through its valence state of + 4, M-NS can generate • OH and other oxidizing agents in response to H_2O_2 and H^+ in the tumor microenvironment. This kind of Fenton reaction induces oxidative stress within the tumor so that highly toxic • OH is used to kill cancer [26, 43]. To evaluate the nanocatalysis efficacy possessed by Zeb@MH-NS, electron spin resonance (ESR) was used to verify that Zeb@MH-NS could generate ROS with potent cytotoxic effects, including the detection of characteristic • OH signal peaks (1:2:2:1) were captured under H_2O_2-rich TEM (Fig. 2D); Additionally, the breakdown of methylene blue (MB) in the presence of Zeb@MH-NS (1 mg/ml) and varying concentrations of H_2O_2 was observed, evidenced by the reduction of MB's characteristic UV absorption peak at 665 nm(Fig. S10A and S10B). we verify the absorbance change of MB with time after mixing Zeb@M-NS and Zeb@MH-NS with MB, as shown in Fig. S10B, no obvious degradation was observed when mixing nano-modulators with MB. However, its UV absorption peak showed that nano-modulators mixed with MB, as well as MB alone, also showed slight MB degradation efficacy after preventing the placement in the air for different times, especially after the simulated tumor microenvironment enriched with H_2O_2, the nano-modulators produced higher concentrations of ROS. At the cut-off time (3 h), the blue color of Zeb@MH-NS + H_2O_2 + MB was explained to become a light blue liquid compared

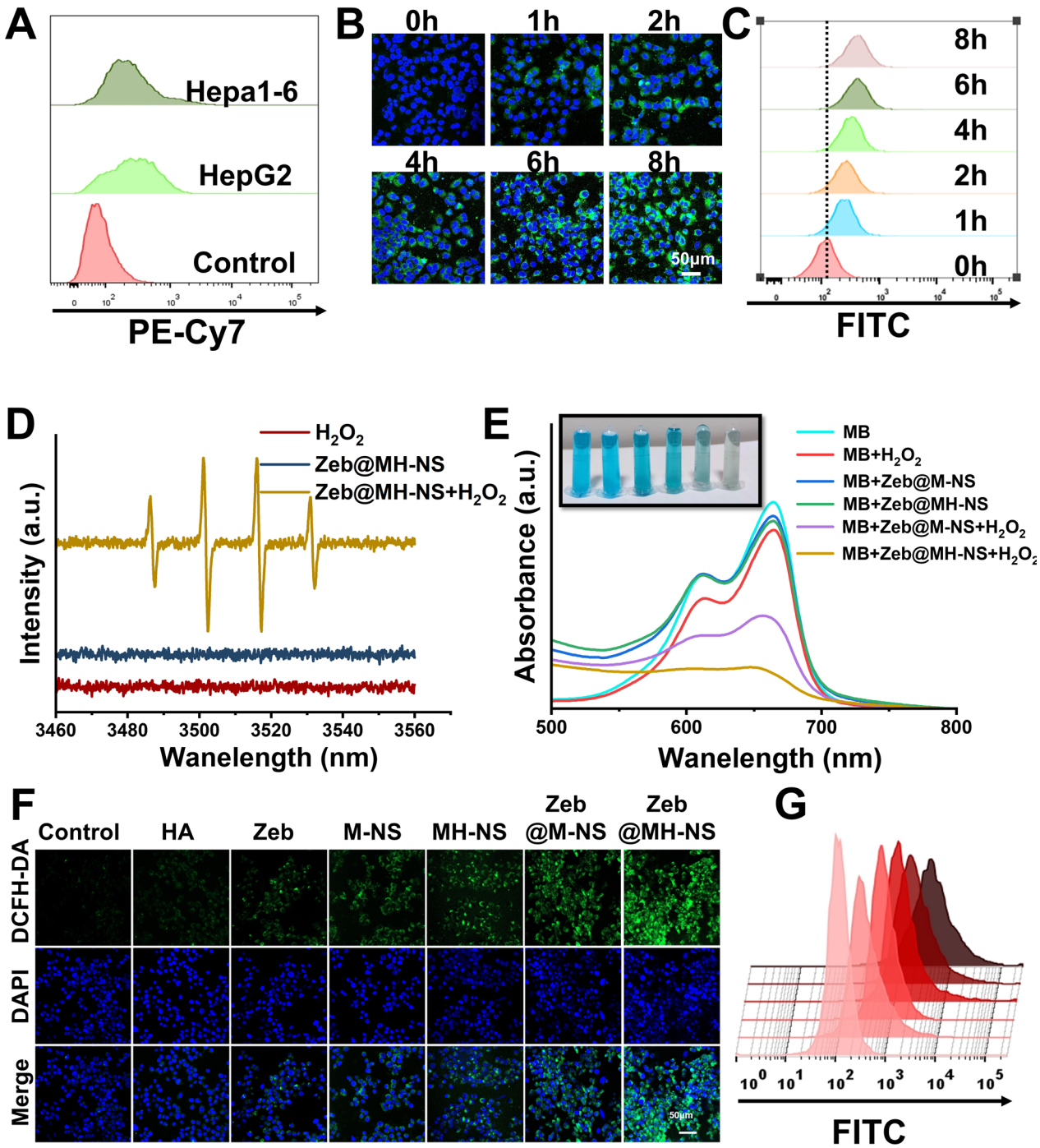

Fig. 2 In vitro assessment of the targeting of Zeb@MH-NS and the mechanism of ROS generation (A) Comparison of CD44 receptor expression on the membrane surface of murine-derived Hepa1-6 and human-derived HepG2 cells. (B) CLSM images of Hepa1-6 cells after incubation with FITC-labelled Zeb@MH-NS nanoparticles for different periods (scar bar: 50 μm) and (C) FCM quantitative analysis of fluorescence intensity changes. (D) Zeb@MH-NS produces ESR spectra of • OH (E) UV–Vis of MB degradation by Zeb@MH-NS and Zeb@M-NS in H_2O_2 (200 mM). (F) CLSM images of ROS production in Hepa1-6 cells stained with ROS indicator after different corresponding treatments (scar bar: 50 μm) and (G) corresponding fluorescence intensity analyzed by FCM

to Zeb@MH-NS + MB, whereas the blue color of Zeb@MH-NS + MB was still clearly visible (Fig. 2E). Notably, the combination of • OH generated by the reaction and the catalytic action of the nano-modulator degraded the MB solution more significantly when co-incubated with 200 mM H_2O_2 (Fig. 2E). Subsequently, the nanocatalytic properties and oxidative stress-breaking ability of Zeb@MH-NS were further verified at the in vitro level to kill tumor cells[44]. Zeb@MH-NS induced distinct green ROS fluorescence in Hepa1-6 cells as detected by CLSM through 2′,7′-Dichlorofluorescin diacetate (DCFH-DA) as a ROS indicator (Fig. 2F); FCM quantification of intracellular ROS levels in the presence of nano-modulator showed that all groups containing M-NS produced ROS, with Zeb@MH-NS yielding the highest levels (Fig. 2G and S8B). These findings underscore Zeb@MH-NS's potent catalytic performance, establishing a foundation for its use in catalytic nano-modulator treatments.

Mechanisms by which Zeb@MH-NS remodels intracellular oxidative stress and induces cellular damage

In tumor-specific microenvironments, the activation of intra- and extracellular stress signals can trigger programmed cell death, which is closely associated with cancer development, malignant progression, and treatment resistance [45]. Numerous studies have established a strong link between mitochondria and cell death [46, 47]. Employing JC-1 to assess the mitochondrial membrane potential, we observed that normal Hepa1-6 cells demonstrated increased accumulation and multimerization of JC-1 within the mitochondria, indicated by enhanced red fluorescence. Conversely, Hepa1-6 treated with Zeb@MH-NS, JC-1 was observed dispersing into the cytoplasm as monomers, marked by an increase in green fluorescence and a corresponding decrease in red fluorescence, as confirmed by both CLSM and FCM (Fig. 3A, B). This shift suggests that Zeb@MH-NS can respond to the tumor microenvironment, producing large amounts of ROS. When the mitochondrial membrane potential is polarized, JC-1 disperses into the mitochondrial matrix, leading to diminished red fluorescence and increased green fluorescence within the cytoplasm as it exists as a monomer.

To find out if apoptotic cascade response could be aided by mitochondrial membrane potential malfunction, which was noted under CLSM that Zeb@M-NS and Zeb@MH-NS, particularly when combined with M-NS, Zeb, and HA in the antitumor nano-modulator, triggered significant cell death, as evidenced by calcein acetylmethoxylate/propidium iodide (Calcein-AM/PI) staining (Fig. 3F). This observation aligns with apoptosis rate findings from FCM, showing that Zeb@MH-NS markedly increased apoptosis in Hepa1-6 cells (Fig. 3C, D, and E). Additionally, a quantitative in vitro antitumor assay using the CCK8 method revealed a significant reduction in cell survival in the Zeb@MH-NS group (Fig. S11). To further explore that mitochondrial membrane potential damage suggested that this dysfunction might induce an irreversible apoptotic program in cancer cells, as evidenced by Western blot (WB) analysis, which revealed elevated levels of pro-apoptotic proteins Bax and Caspase 3 and reduced levels of the anti-apoptotic protein Bcl-2 in the Zeb@MH-NS treated group (Fig. 3F and Fig. S13B).

In vivo antitumor effects of Zeb@MH-NS

Inspired by the tumor microenvironment-responsive nanocatalysis of Zeb@MH-NS in vitro studies, which impaired mitochondrial membrane potential and induced apoptosis, Zeb@MH-NS was designed and evaluated for its antitumor ability in Hepa1-6 loaded C57BL/6 J mouse, and the process is shown in Fig. 4A. Treatment with Zeb@MH-NS resulted in significant tumor growth inhibition, as evidenced by the reduction in tumor volume throughout treatment (Fig. 4B, C). The weight of mouse were checked every three days to evaluate the biosafety of the medication, and there was no discernible decline (Fig. 4D), suggesting that Zeb@MH-NS is biocompatible. Survival analysis conducted over 70 days showed that the survival rate of mice treated with Zeb@MH-NS was significantly higher than that of control groups (Fig. 4E). At the end of the treatment period, the tumor tissues of mice were excised and weighed. The growth of tumor tissues of Zeb@MH-NS and Zeb@MH-NS treated significant Hepa1-6 tumor-bearing mice, whose tumor weight was significantly reduced (Fig. 4F). The tumor tissues of the different subgroups were subjected to tumor sections for hematoxylin–eosin (H&E) staining, Tunnel, and Ki67 assays across several subgroups, it was observed that the Zeb@MH-NS therapy led to a notable alteration in the tumor cell arrangement, which became more dispersed. Additionally, the nuclei within these cells appeared condensed and segmented, while the cytoplasm shifted toward a reddish hue, particularly when contrasted with the control group. The intensity of the red fluorescence of the Ki67 expression was also significantly reduced. The antitumor solid ability of Zeb@MH-NS led to programmed cell death. Therefore, during Tunnel staining (Fig. 4G), fluorescein-labelled dUTP in tumor tissues ligates with the 3'-OH terminus of broken DNA in apoptotic cancer cells, reacting with the HRP substrate diaminobenzidine (DAB) to produce significant green fluorescence intensity [48–50]. Combined with the WB analysis of the extracted proteins from the tumor tissues, the expression of apoptotic proteins was similar to the WB analysis of the cellular experiments (Fig. 4H), which implies that inhibition of cell proliferation and promotion

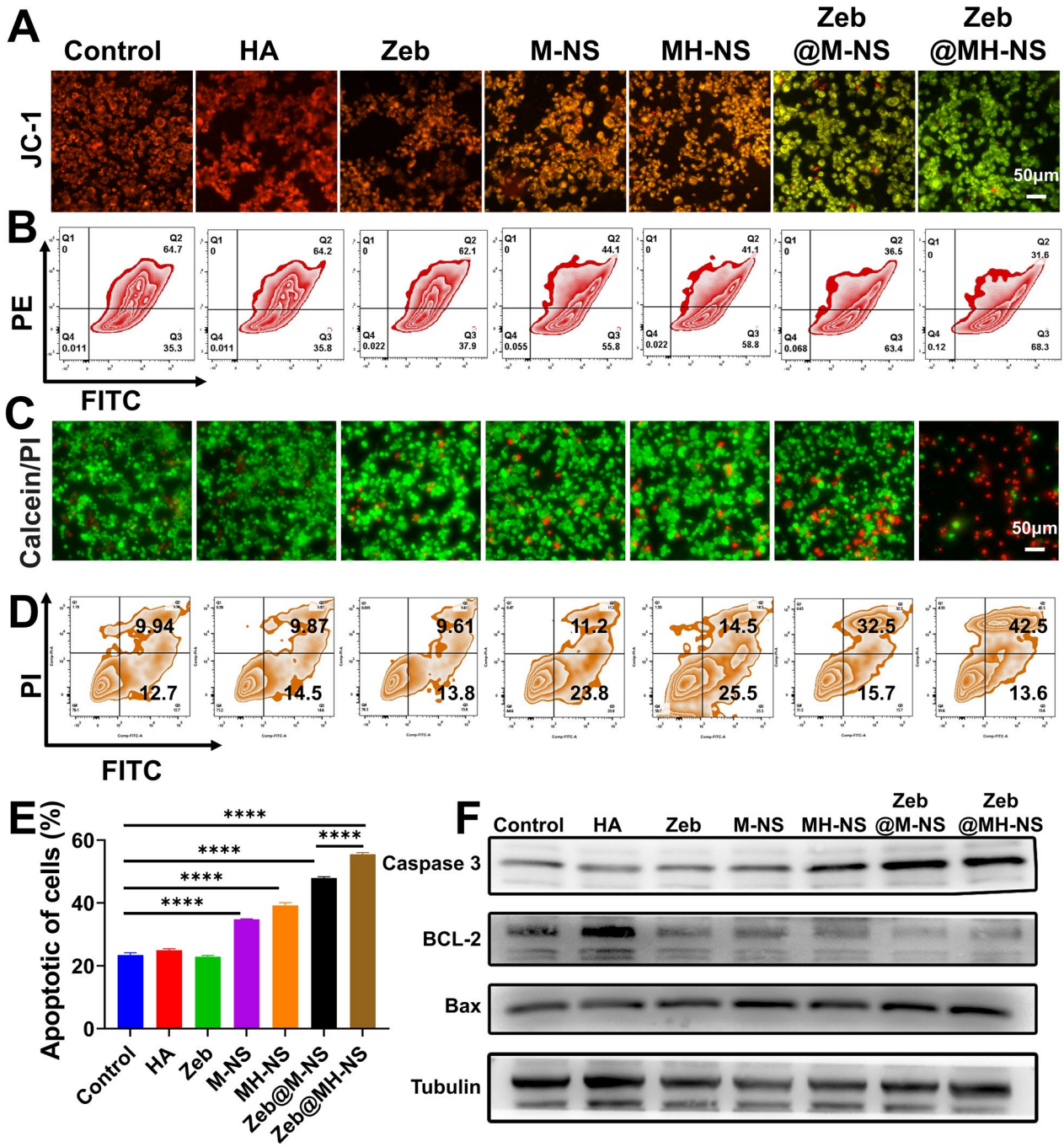

Fig. 3 In vitro assessment of the antitumor properties of Zeb@MH-NS. (A) CLSM images of mitochondrial dysfunction in Hepa1-6 cells were assessed using JC-1 (aggregates in red, monomers in green) after different treatments (scar bar: 50 μm) and (B) FCM analysis of the decrease in mitochondrial membrane potential. (C) CLSM images of Hepa1-6 cells co-stained with calcein AM/PI after different corresponding treatments (scar bar: 50 μm) (D) FCM and (E) relative quantitative analysis of apoptotic double staining of Hepa1-6 cells with AnnexinV-FITC/PI after different treatments. (F) WB bands of Hepa1-6 cells after different treatments for detecting apoptosis-related protein expression levels. (*$p < 0.05$, **$p < 0.01$, ***$p < 0.001$, ****$p < 0.0001$)

of cell death is responsible for the significant shrinkage of the tumor (Fig. 4G) and that Zeb@MH-NS synthesized in the study has an excellent antitumor therapy.

Zeb@MH-NS activates innate immunity via the cGAS-STING signalling pathway for tumor elimination

M-NS can act as a nanocatalyst in antitumor therapy.

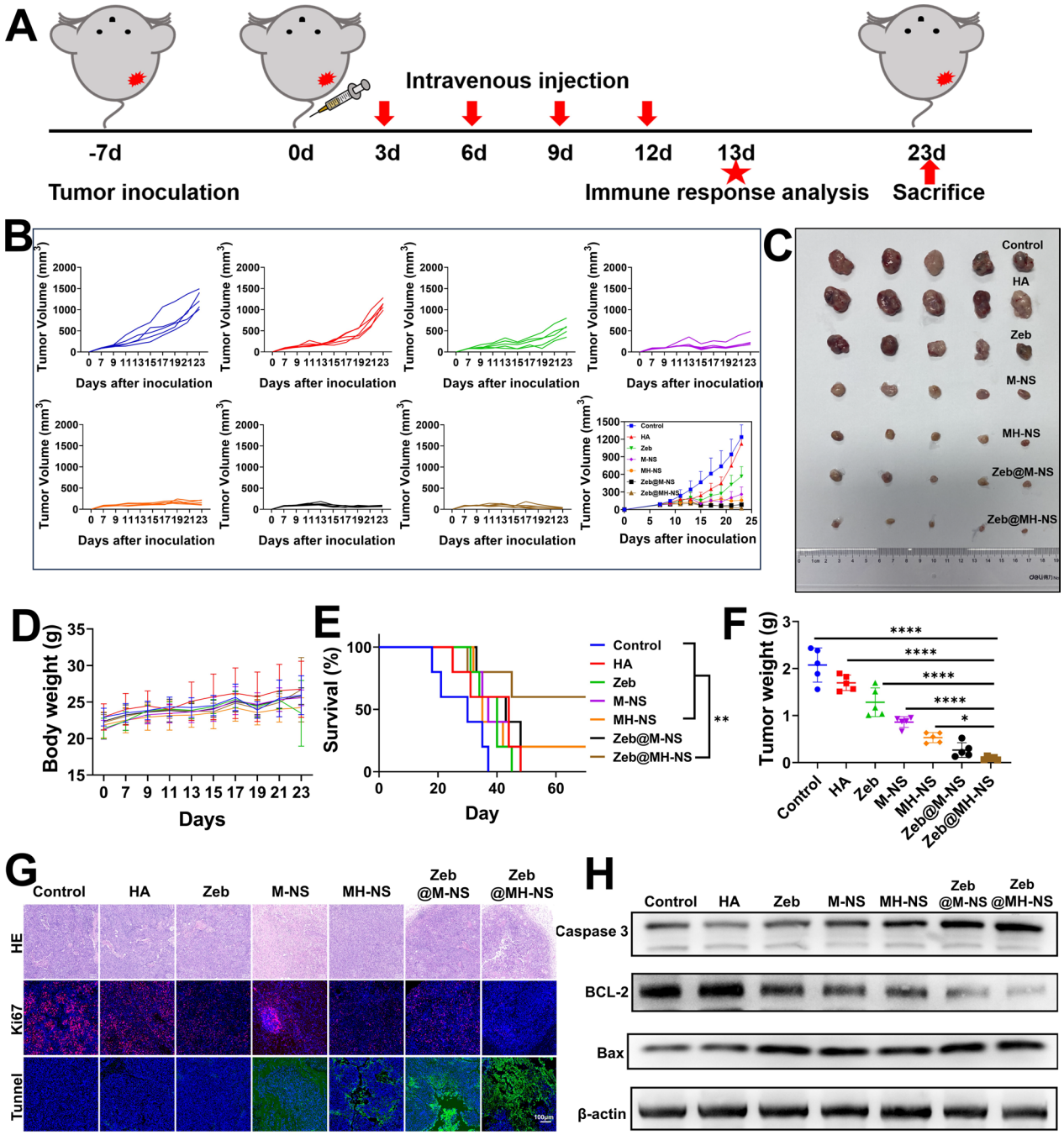

Fig. 4 In vivo assessment of antitumor properties of Zeb@MH-NS. (A) Schematic diagram of the experimental design for the in vivo evaluation of the antitumor properties of Zeb@MH-NS and its triggered immune response. (B) Detailed tumor growth curves and tumor volume change curves over time in different groups of ruffed mice after different treatments (including the control group, the HA group, the Zeb group, the M-NS group, the MH-NS group, the Zeb@M-NS group, the Zeb@MH-NS group). (C) Photographs of the tumors of the ruffled mice after different treatments (n = 5). (D) Curves of the body weight of the tumor-bearing mice after different treatments (n = 5). (E) Survival curves of the tumor-bearing mice after different treatments (n = 5). (F) Changes in the weight of the tumors of the tumor-bearing mice after different treatments (n = 5). (G) The tumor slices of the tumor-bearing mice after different treatments were stained for H&E, TUNEL, and Ki67 staining. (H) The expression of apoptosis-related proteins in tumor tissues after different treatments (n = 5). (*p < 0.05, **p < 0.01, ***p < 0.001, ****p < 0.0001)

Under the dual catalysis of H^+ and H_2O_2 in the TME, manganese transitions from a + 4 valence to a + 2 valence, undergoing a Fenton-like reaction to produce ROS. This reaction damages mitochondria and induces apoptosis in tumor cells [39, 51]. Moreover, Mn^{2+} can enhance the activity of the cytoplasmic cGAS-STING signalling cascade, facilitate the secretion of pro-inflammatory mediators, and stimulate the tumor's immune milieu via manganese-based immunotherapy, exhibiting significant antineoplastic properties [52]. The combination of Zeb sensitizing the cGAS-STING pathway with manganese dioxide amplifies the potency of innate immunity. This enhancement activates immune cells across various levels of the immune system by boosting the expression of the cGAS-STING pathway, thus maximizing the tumor-killing effect (Fig. 5A). To assess the impact of Zeb@MH-NS on innate immunity activation, we analyzed the expression of cGAS-STING pathway-related proteins and their downstream phosphorylated counterparts at both in vitro and in vivo levels after treatment. WB results indicated that, compared to other groups, the Zeb@MH-NS group showed a responsive release of more Mn^{2+} from the tumor microenvironment and direct DNA damage by Zeb, stimulating cGAS expression. Additionally, mitochondrial dysfunction led to mtDNA leakage, further enhancing the activation of the STING pathway and associated phosphorylated proteins [46, 53]. The expression of phosphorylated STING (pSTING), TBK1 (pTBK1), and IRF3 (pIRF3) was significantly elevated (Fig. 5B and Fig. S13 A-D), indicating that Zeb/ROS/Mn^{2+} release triggered by the tumor microenvironment substantially activates the cGAS-STING channel and boosts STING-induced type I interferon production. Subsequent evaluations showed that pro-inflammatory cytokines, including interferon-γ (IFN-γ), tumor necrosis factor-alpha (TNF-α), and interleukin 6 (IL-6), were elevated in the Zeb@MH-NS cohort (Fig. 5G), implying that the activation of the cGAS-STING pathway has the potential to convert "cold" tumors into more sensitive "hot" tumors.

IFN, a downstream signal of the cGAS-STING signalling pathway, is pivotal in bridging innate and adaptive immunity. It contributes to the maturation and migration of DCs, enhances the cytotoxicity mediated by CTLs or NKs, and promotes the polarization of macrophages into M1-type macrophages [54–56]. To verify the activating effect of Zeb@MH-NS on innate immunity (Fig. S14), tumor tissues of mice in each group were taken one day after the end of drug treatment for immune response analysis, and the expression of mature DCs ($CD11c^+MHC\text{-}II^+CD80^+CD86^+$) was significantly enhanced in Hepa1-6 tumors of the Zeb@MH-NS group as compared to the other groups (Fig. 5C); Similarly, Zeb@MH-NS treatment resulted in a notable increase in the intratumoral abundance of pro-inflammatory M1-like TAM ($CD11b^+F4/80^+$ $CD80^+CD86^+$) (Fig. 5D), indicative of a robust immune response. In addition, treatment with Zeb@MH-NS could promote NK cells ($CD11b^{\pm}NK1.1^+$) by promoting to activate of the innate immune response (Fig. 5E) and efficiently induce the acquired immune response by promoting total tumor T cells ($CD3^+$) and their activation ($CD3^+CD69^+$). Although the Zeb@M-NS group also promoted the infiltration and activation of T cells, the effect was less pronounced compared to the Zeb@MH-NS group, likely due to the targeted modifications conferred by HA in Zeb@MH-NS (Fig. S15A-F).

Furthermore, Zeb@MH-NS treatment proved to be the most effective in promoting intratumoral cytotoxic T cell (CTL, $CD3^+CD8^+IFN\gamma^+$) abundance (Fig. 5F), which is one of the most critical indicators of adaptive antitumor immune activation [57, 58]. Blood serum samples were obtained post-treatment from different mice cohorts and evaluated for TNF-α, IFN-γ, and IL-6 levels to assess the start of the cGAS-STING signalling cascade and its impact on cytokine production within tumors. The elevated cytokine levels confirmed the activation of the cGAS-STING pathway alongside the activation of effector T cells, NK cells, and M1 macrophages associated with these cytokines (Fig. 5G and S15).

Additionally, we validated its ability to induce immunogenic cell death (ICD) at the ex vivo and in vivo levels. When cells undergo ICD, the high mobility group 1 (HMGB1) protein (Figure S12B), secreted adenosine triphosphate (ATP) (Figure S12D), and surface-exposed calreticulin (CRT) are released (Figure S12C). After treatment, we examined the main immunogenic features of ICDs from different treatment groups by examining tumor tissue sections from hepatocellular carcinoma cells in vitro and in vivo. Compared with the control group, the Zeb@MH-NS-treated group showed low expression levels of cytoplasmic HMGB1 green fluorescence intensity and low intracellular ATP content due to the intracellular release of HMGB1 and ATP (Figure S12B, S12D); however, the level of CRT exposed on the surface of the tumor cells was high (Figure S12C), which was consistent with the detection of CRT expression after the treatment in mice in vivo (Figure S12E, S12F). Combined with our previous flow exploration of immune activation in vivo, it is suggested that our constructed nano-agonist Zeb@MH-NS promotes ICD during saprophytic cell death, generates new antigenic epitopes and releases damage-associated molecular patterns (DAMPs) from dead cells, recruits antigen-presenting cells to recognize and phagocytose dead cell antigens and present them to T cells, activating adaptive immune response to

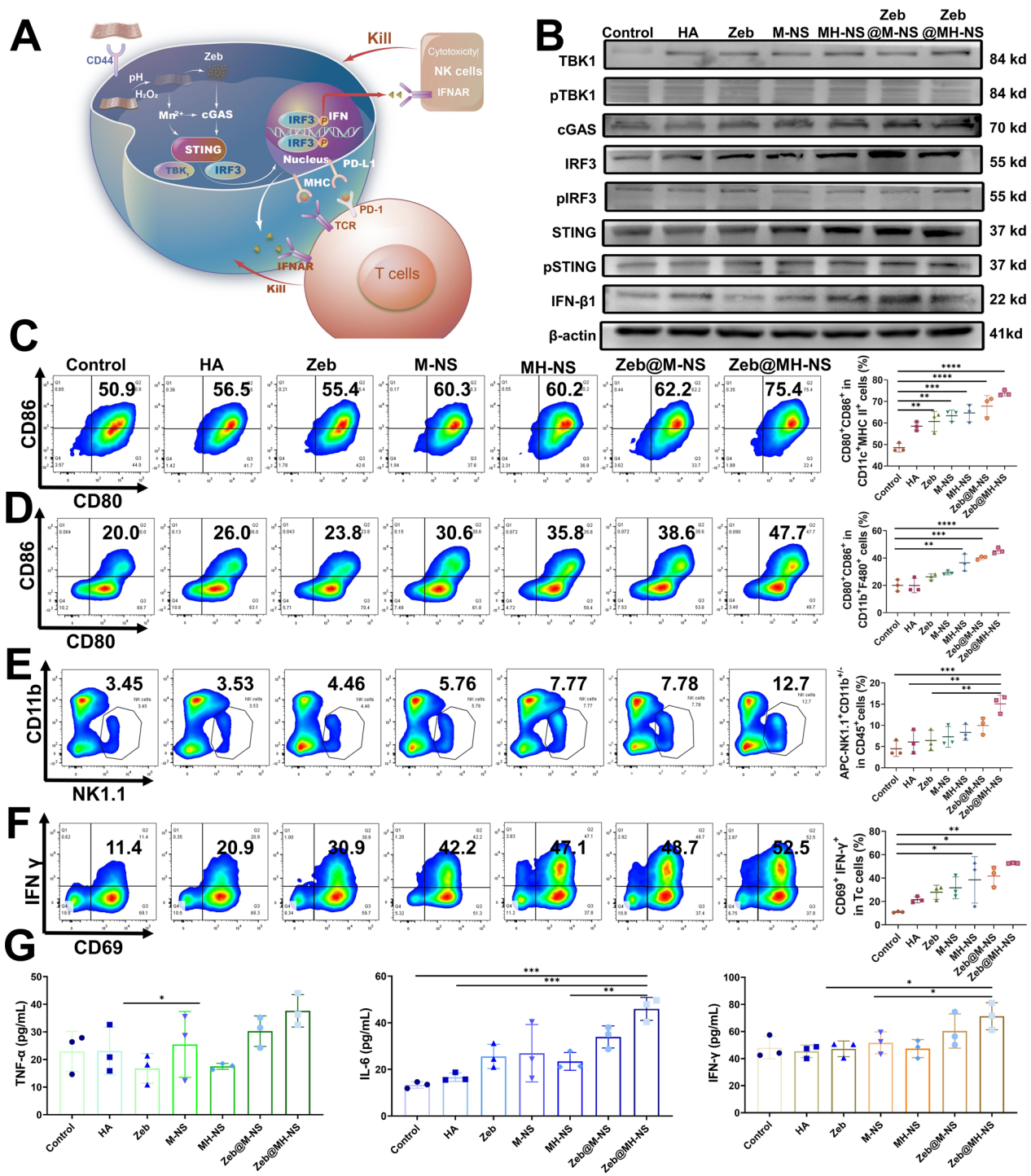

Fig. 5 Assessment of antitumor immune response and mechanism of Zeb@MH-NS in vivo. (A) Brief schematic diagram of activating a cGAS-STING signalling pathway to generate an immune response by Zeb@MH-NS in hormonal mice. (B) WB is used to detect STING, TBK1, IRF3, and their corresponding phosphorylated proteins in the tumor tissues. (C) FCM to detect the DC in Hepa1-6 tumor tissues after different treatments ($CD11c^{+}MHCII^{+}CD80^{+}CD86^{+}$) expression after different treatments. (D) FCM to detect the expression of M1-type macrophages ($CD11b^{+}F480^{+}CD80^{+}CD86^{+}$) in Hepa1-6 tumor tissues after different treatments. (E) FCM to detect NK cells ($CD45^{+}APC\text{-}NK1.1^{+}$ $CD11b^{\pm}$) expression. (F) FCM to detect the expression of activated CTL ($CD3^{+}CD8^{+}CD69^{+}IFN\text{-}\gamma.^{+}$) in Hepa1-6 tumor tissues after different treatments. (G) After different treatments, expression levels of TNF-α, IL 6, and IFN γ in Hepa1-6 tumor tissues. (*$p < 0.05$, **$p < 0.01$, ***$p < 0.001$, ****$p < 0.0001$)

recognize and clear tumor antigens, which will be able to produce long-lasting anti-tumour immune effects. These findings collectively demonstrate that Zeb@MH-NS acts as a potent cGAS stimulator, effectively reversing tumor immunosuppression by enhancing innate and acquired immune responses.

Biodistribution and biosafety evaluation of Zeb@MH-NS

Zeb@MH-NS nanoparticles were combined with blood cells at different doses to measure the hemolysis rate and determine the particles' biosafety in a mouse model. Even at a 100 μg/mL concentration, the hemolysis rate remained below 5% (Fig. S16). Following the administration of nanotherapeutics to different treatment groups, examinations of primary organ tissues, including the heart, liver, spleen, lungs, and kidneys, which harvested from mice, revealed no significant pathologic alterations with hematoxylin and eosin staining (Fig. S17). Additionally, serum biochemical analyses (Fig. S18) and body weight measurements (Fig. S16B) showed no significant changes, indicating good histocompatibility of Zeb@MH-NS in vivo.

Further analysis of the targeting and biodistribution of Zeb@MH-NS compared to Zeb@M-NS was conducted. The fluorescence intensity of Cy5.5-labeled nanoparticles was tracked using an IVIS spectral imaging system (Fig. S19A) to evaluate their distribution and tumor accumulation in Hepa1-6 tumor-bearing mice. The fluorescence intensity in the tumor region increased over time, reaching a peak six hours post-injection. Semi-quantitative biodistribution studies involving the isolation of significant organs demonstrated that Zeb@MH-NS exhibited higher tumor uptake and retention than Zeb@M-NS (Fig. S19A-C). Notably, considerable fluorescence was also observed in the liver and kidneys, which are critical for the degradation and excretion of the nanoparticles, indicating active processing by the somatic circulation (Fig. S19D).

Conclusions

M-NS responds to H^+ in the TME by remodelling it and catalyzing the conversion of H_2O_2 into quantities of ROS, which damages mitochondria and promotes irreversible cellular damage. This biomineralization strategy employs M-NS as carriers that activate the intracellular cGAS-STING signaling pathway and the drug Zeb. In response to the TME, Mn^{2+} is catabolized to augment programmed cell death and immune response. After combining the targeted surface modification of Zeb and HA, Zeb@MH-NS, a nano-modulator with a targeted CD44 receptor, can cascade activation of the cGAS-STING signalling pathway. This activation and the subsequent mobilization of immune system components transform "cold tumors" into "hot tumors," enhancing intracellular and extracellular anticancer effects and ultimately promoting cell death and immune response.

Supplementary Information

The online version contains supplementary material available at https://doi.org/10.1186/s12951-024-02809-6.

Additional file 1: The supporting information includes materials, characterizations, and supplementary figures S1-S19.

Acknowledgements

Not applicable.

Author contributions

X.L., D.W., and Y.Z. contributed equally to this study. S.Y., W.H., Y.Y., X.L., D.W., and S.Y. proposed the research direction, and X.D., L.Z., J.Y., X.L., X.D., and D.W. designed the content and planning of this study. X.L., D.W., S.Y., Y.Z., W.H., Y.Y., X.W., X.D., L.Z., and J.Y. were involved in the operation and protocol design of cell and animal experiments throughout the experimental process; X.W., X.L., D.W., Y.Z., W.H., were involved in the collection, analysis, and collation of the data. X.L., Y.Z., S.Y., and L.Z. were responsible for the experiment flow, and the data were related to statistics and analysis using software. Meanwhile, the first draft of the paper was prepared by X.L., D.W., and Y.Z., and the manuscript was reviewed and revised by J.Y., L.Z., and X.D.

Funding

This work was partially supported by the National Natural Science Foundation of China (No. 82260345, No. 82360569, No. 82160589 and No. 82302330), Guangxi Science and Technology Major Project (GuikeAA23073013), Research Personnel Cultivation Programme of Zhongda Hospital Southeast University (CZXM-GSP-RC81), Postdoctoral Fellowship Program of CPSF (BX20230068), China Postdoctoral Science Foundation (2024M750452).

Availability of data and materials

The data that support the findings of this study are available from the corresponding author upon reasonable request.

Declarations

Ethics approval and consent to participate

All experimental procedures involving animals and patients were conducted per institutional guidelines and approved by the Laboratory Animal Center of Guangxi Medical University (LW2024068), Guangxi Key Laboratory of Early Prevention and Treatment for Regional High Frequency Tumor, and Tumor Hospital of Guangxi Medical University.

Competing interests

The authors declare no competing interests.

Author details

[1]Department of Hepatobiliary Surgery, Department of Medical Ultrasound, Tumor Hospital of Guangxi Medical University, Guangxi Medical University, No. 71 Hedi Road, Nanning 530021, Guangxi, China. [2]Center of Interventional Radiology & Vascular Surgery, Department of Radiology, Zhongda Hospital, Medical School, Southeast University, Nanjing 224001, China. [3]Department of Hepatobiliary, Pancreas and Spleen Surgery, the People's Hospital of Guangxi Zhuang Autonomous Region, Guangxi Academy of Medical Sciences, Nanning 530021, China.

Received: 2 June 2024 Accepted: 22 August 2024
Published online: 03 September 2024

References

1. Wu S, Zhang Q, Zhang F, Meng F, Liu S, Zhou R, Wu Q, Li X, Shen L, Huang J. HER2 recruits AKT1 to disrupt STING signalling and suppress antiviral defence and antitumour immunity. Nat Cell Biol. 2019;21(8):1027–40.
2. Fang R, Jiang Q, Guan Y, Gao P, Zhang R, Zhao Z, Jiang Z. Golgi apparatus-synthesized sulfated glycosaminoglycans mediate polymerization and activation of the cGAMP sensor STING. Immunity. 2021;54(5):962–75.
3. Yu X, Zhang L, Shen J, Zhai Y, Jiang Q, Yi M, Deng X, Ruan Z, Fang R, Chen Z. The STING phase-separator suppresses innate immune signalling. Nat Cell Biol. 2021;23(4):330–40.
4. Lv M, Chen M, Zhang R, Zhang W, Wang C, Zhang Y, Wei X, Guan Y, Liu J, Feng K. Manganese is critical for antitumor immune responses via cGAS-STING and improves the efficacy of clinical immunotherapy. Cell Res. 2020;30(11):966–79.
5. Wang D, Zhou J, Fang W, Huang C, Chen Z, Fan M, Zhang M-R, Xiao Z, Hu K, Luo L. A multifunctional nanotheranostic agent potentiates erlotinib to EGFR wild-type non-small cell lung cancer. Bioactive Mater. 2022;13:312–23.
6. Ning X, Wang Y, Jing M, Sha M, Lv M, Gao P, Zhang R, Huang X, Feng J-M, Jiang Z. Apoptotic caspases suppress type I interferon production via the cleavage of cGAS, MAVS, and IRF3. Mol Cell. 2019;74(1):19–31.
7. Wang C, Guan Y, Lv M, Zhang R, Guo Z, Wei X, Du X, Yang J, Li T, Wan Y. Manganese increases the sensitivity of the cGAS-STING pathway for double-stranded DNA and is required for the host defense against DNA viruses. Immunity. 2018;48(4):675–87.
8. Wang Y, Ning X, Gao P, Wu S, Sha M, Lv M, Zhou X, Gao J, Fang R, Meng G. Inflammasome activation triggers caspase-1-mediated cleavage of cGAS to regulate responses to DNA virus infection. Immunity. 2017;46(3):393–404.
9. Wang D, Nie T, Huang C, Chen Z, Ma X, Fang W, Huang Y, Luo L, Xiao Z. Metal-cyclic dinucleotide nanomodulator-stimulated STING signaling for strengthened radioimmunotherapy of large tumor. Small. 2022;18(41):2203227.
10. Tian H, Wang G, Sang W, Xie L, Zhang Z, Li W, Yan J, Tian Y, Li J, Li B. Manganese-phenolic nanoadjuvant combines sonodynamic therapy with cGAS-STING activation for enhanced cancer immunotherapy. Nano Today. 2022;43: 101405.
11. Wang C, Sun Z, Zhao C, Zhang Z, Wang H, Liu Y, Guo Y, Zhang B, Gu L, Yu Y. Maintaining manganese in tumor to activate cGAS-STING pathway evokes a robust abscopal antitumor effect. J Control Release. 2021;331:480–90.
12. Zhao Z, Ma Z, Wang B, Guan Y, Su X-D, Jiang Z. Mn2+ directly activates cGAS and structural analysis suggests Mn2+ induces a noncanonical catalytic synthesis of 2′ 3′-cGAMP. Cell Rep. 2020. https://doi.org/10.1016/j.celrep.2020.108053.
13. Zhang R, Wang C, Guan Y, Wei X, Sha M, Yi M, Jing M, Lv M, Guo W, Xu J. Manganese salts function as potent adjuvants. Cell Mol Immunol. 2021;18(5):1222–34.
14. Yu M, Duan X, Cai Y, Zhang F, Jiang S, Han S, Shen J, Shuai X. Multifunctional nanoregulator reshapes immune microenvironment and enhances immune memory for tumor immunotherapy. Adv Sci. 2019;6(16):1900037.
15. Guan X, Sun L, Shen Y, Jin F, Bo X, Zhu C, Han X, Li X, Chen Y, Xu H. Nanoparticle-enhanced radiotherapy synergizes with PD-L1 blockade to limit post-surgical cancer recurrence and metastasis. Nat Commun. 2022;13(1):2834.
16. Wang D, Feng C, Xiao Z, Huang C, Chen Z, Fang W, Ma X, Wang X, Luo L, Hu K. Therapeutic hydrogel for enhanced immunotherapy: a powerful combination of MnO2 nanosheets and vascular disruption. Nano Today. 2022;47: 101673.
17. Lai J, Fu Y, Tian S, Huang S, Luo X, Lin L, Zhang X, Wang H, Lin Z, Zhao H. Zebularine elevates STING expression and enhances cGAMP cancer immunotherapy in mice. Mol Ther. 2021;29(5):1758–71.
18. Cho W, Lee JH, S.B. Park, STING upregulation strategies to potentiate STING immunotherapy. Future Med Chem. 2023;15(20):1819–22.
19. Zhang J, Yu S, Peng Q, Wang P, Fang L. Emerging mechanisms and implications of cGAS-STING signaling in cancer immunotherapy strategies. Cancer Biol Med. 2024;21(1):45.
20. Tripathi S, Najem H, Mahajan AS, Zhang P, Low JT, Stegh AH, Curran MA, Ashley DM, James CD, Heimberger AB. cGAS-STING pathway targeted therapies and their applications in the treatment of high-grade glioma. F1000Res. 2022. https://doi.org/10.12688/f1000research.125163.1.
21. Taffoni C, Schüssler M, Vila IK, Laguette N. Harnessing the cooperation between DNA-PK and cGAS in cancer therapies: the cooperation between DNA-PK and cGAS shapes tumour immunogenicity. J BioEssays. 2023;45(7):2300045.
22. Ruan H, Hu Q, Wen D, Chen Q, Chen G, Lu Y, Wang J, Cheng H, Lu W, Gu Z. A dual-bioresponsive drug-delivery depot for combination of epigenetic modulation and immune checkpoint blockade. Adv Mater. 2019;31(17):1806957.
23. Liang X, Zhang Y, Zhou J, Bu Z, Liu J, Zhang K. Tumor microenvironment-triggered intratumoral in situ construction of theranostic supramolecular self-assembly. Coordin Chem Rev. 2022;473: 214824.
24. Wang D, Zhang M, Zhang Y, Qiu G, Chen J, Zhu X, Kong C, Lu X, Liang X, Duan L. Intraparticle double-scattering-decoded sonogenetics for augmenting immune checkpoint blockade and CAR-T therapy. Advanced Science. 2022;9(32):2203106.
25. Wang Y, Li Y, Zhang Z, Wang L, Wang D, Tang BZ. Triple-jump photodynamic theranostics: MnO2 combined upconversion nanoplatforms involving a type-i photosensitizer with aggregation-induced emission characteristics for potent cancer treatment. Adv Mater. 2021;33(41):2103748.
26. Fan W, Bu W, Shen B, He Q, Cui Z, Liu Y, Zheng X, Zhao K, Shi J. Intelligent MnO 2 nanosheets anchored with upconversion nanoprobes for concurrent pH-/H 2 O 2-responsive UCL imaging and oxygen-elevated synergetic therapy. Adv Mater. 2015;28(27):4155–61.
27. He T, Xu H, Zhang Y, Yi S, Cui R, Xing S, Wei C, Lin J, Huang P. Glucose oxidase-instructed traceable self-oxygenation/hyperthermia dually enhanced cancer starvation therapy. Theranostics. 2020;10(4):1544.
28. Selvakumar K, Kumar SS, Thangamuthu R, Kruthika G, Murugan P. Development of shape-engineered α-MnO2 materials as bi-functional catalysts for oxygen evolution reaction and oxygen reduction reaction in alkaline medium. Int J Hydrogen Energy. 2014;39(36):21024–36.
29. Zhang X, Tang J, Li C, Lu Y, Cheng L, Liu J. A targeting black phosphorus nanoparticle based immune cells nano-regulator for photodynamic/photothermal and photo-immunotherapy. Bioact Mater. 2021;6(2):472–89.
30. Guo Y, Wang S-Z, Zhang X, Jia H-R, Zhu Y-X, Zhang X, Gao G, Jiang Y-W, Li C, Chen X. In situ generation of micrometer-sized tumor cell-derived vesicles as autologous cancer vaccines for boosting systemic immune responses. Nat Commun. 2022;13(1):6534.
31. Wang B, Wang T, Jiang T, Li S, Zhang L, Zhao X, Yang X, Wang X. Circulating immunotherapy strategy based on pyroptosis and STING pathway: Mn-loaded paclitaxel prodrug nanoplatform against tumor progression and metastasis. Biomaterials. 2024;306: 122472.
32. Yang HY, Jang M-S, Sun XS, Liu CL, Lee JH, Li Y, Fu Y. CD44-mediated tumor homing of hyaluronic acid nanogels for hypoxia-activated photodynamic therapy against tumor. Colloids Surf B Biointerfaces. 2023;228: 113395.
33. Jiang C, He T, Tang Q, He J, Ren Q, Zhang D-Y, Gurram B, Blum NT, Chen Y, Huang P. Nanozyme catalyzed cascade reaction for enhanced chemodynamic therapy of low-H2O2 tumor. Appl Mater Today. 2022;26: 101357.
34. Deng Z, Xi M, Zhang C, Wu X, Li Q, Wang C, Fang H, Sun G, Zhang Y, Yang G. Biomineralized MnO2 nanoplatforms mediated delivery of immune checkpoint inhibitors with STING pathway activation to potentiate cancer radio-immunotherapy. ACS Nano. 2023;17(5):4495–506.
35. Zhang J, Xu M, Mu Y, Li J, Foda MF, Zhang W, Han K, Han H. Reasonably retard O2 consumption through a photoactivity conversion nanocomposite for oxygenated photodynamic therapy. Biomaterials. 2019;218: 119312.
36. Sun Z, Wang Z, Wang T, Wang J, Zhang H, Li Z, Wang S, Sheng F, Yu J, Hou Y. Biodegradable MnO-based nanoparticles with engineering surface for tumor therapy: simultaneous fenton-like ion delivery and immune activation. ACS Nano. 2022;16(8):11862–75.
37. Zhou Q, Dutta D, Cao Y, Ge Z. Oxidation-responsive PolyMOF nanoparticles for combination photodynamic-immunotherapy with enhanced STING activation. ACS Nano. 2023;17(10):9374–87.
38. Zhao Z, Dong S, Liu Y, Wang J, Ba L, Zhang C, Cao X, Wu C, Yang P. Tumor microenvironment-activable manganese-boosted catalytic immunotherapy combined with PD-1 checkpoint blockade. ACS Nano. 2022;16(12):20400–18.

39. Yang G, Xu L, Chao Y, Xu J, Sun X, Wu Y, Peng R, Liu Z. Hollow MnO2 as a tumor-microenvironment-responsive biodegradable nano-platform for combination therapy favoring antitumor immune responses. Nat Commun. 2017;8(1):902.
40. Wang D, Zhu X, Wang X, Wang Q, Yan K, Zeng G, Qiu G, Jiao R, Lin X, Chen JJAFM. Multichannel sonocatalysis amplifiers target IDH1-mutated tumor plasticity and attenuate ros tolerance to repress malignant cholangiocarcinoma. Adv Funct Mater. 2023;33(48):2303869.
41. Duan S, Xia Y, Tian X, Cui J, Zhang X, Yang Q, Zhao T, Lin Y, Zhang F, Zhang X. A multi-bioresponsive self-assembled nano drug delivery system based on hyaluronic acid and geraniol against liver cancer. Carbohydr Polym. 2023;310: 120695.
42. Son GM, Kim HY, Ryu JH, Chu CW, Kang DH, Park SB, Jeong Y-I. Self-assembled polymeric micelles based on hyaluronic acid-g-poly (D, L-lactide-co-glycolide) copolymer for tumor targeting. Int J Mol Sci. 2014;15(9):16057–68.
43. Liu P, Xie X, Liu M, Hu S, Ding J, Zhou W. A smart MnO2-doped graphene oxide nanosheet for enhanced chemo-photodynamic combinatorial therapy via simultaneous oxygenation and glutathione depletion. Acta Pharm Sin B. 2021;11(3):823–34.
44. Zhu P, Pu Y, Wang M, Wu W, Qin H, Shi J. MnOOH-catalyzed autoxidation of glutathione for reactive oxygen species production and nanocatalytic tumor innate immunotherapy. J Am Chem Soc. 2023;145(10):5803–15.
45. Ganzleben I, Neurath MF, Becker C. Autophagy in cancer therapy—molecular mechanisms and current clinical advances. Cancers. 2021;13(21):5575.
46. Wang K, Li Y, Wang X, Zhang Z, Cao L, Fan X, Wan B, Liu F, Zhang X, He Z. Gas therapy potentiates aggregation-induced emission luminogen-based photoimmunotherapy of poorly immunogenic tumors through cGAS-STING pathway activation. Nat Commun. 2023;14(1):2950.
47. Zhang Y, Zhao J, Zhang L, Zhao Y, Zhang Y, Cheng L, Wang D, Liu C, Zhang M, Fan K. A cascade nanoreactor for enhancing sonodynamic therapy on colorectal cancer via synergistic ROS augment and autophagy blockage. Nano Today. 2023;49: 101798.
48. Hou L, Tian C, Yan Y, Zhang L, Zhang H, Zhang Z. Manganese-based nanoactivator optimizes cancer immunotherapy via enhancing innate immunity. ACS Nano. 2020;14(4):3927–40.
49. Wu H, Wu F, Zhou T, Hu Z, Wang W, Liang X, Wang J, You C, Sun B, Lin F. Activatable autophagy inhibition-primed chemodynamic therapy via targeted sandwich-like two-dimensional nanosheets. Chem Eng J. 2022;431: 133470.
50. Wang D, Zhang M, Qiu G, Rong C, Zhu X, Qin G, Kong C, Zhou J, Liang X, Bu Z. Extracellular matrix viscosity reprogramming by in situ Au bioreactor-boosted microwavegenetics disables tumor escape in CAR-T immunotherapy. ACS Nano. 2023;17(6):5503–16.
51. Zhan M, Wang F, Liu Y, Zhou J, Zhao W, Lu L, Li J, He X. Dual-cascade activatable nanopotentiators reshaping adenosine metabolism for sono-chemodynamic-immunotherapy of deep tumors. Adv Sci. 2023;10(10):2207200.
52. Lu Q, Chen R, Du S, Chen C, Pan Y, Luan X, Yang J, Zeng F, He B, Han X. Activation of the cGAS-STING pathway combined with CRISPR-Cas9 gene editing triggering long-term immunotherapy. Biomaterials. 2022;291: 121871.
53. Tang S, Zhou L, He H, Cui L, Ren Z, Tai Y, Xie Z, Cao Y, Meng D, Liu Q. MnO2-melittin nanoparticles serve as an effective antitumor immunotherapy by enhancing systemic immune response. Biomaterials. 2022;288: 121706.
54. Wang J, Li S, Wang M, Wang X, Chen S, Sun Z, Ren X, Huang G, Sumer BD, Yan N. STING licensing of type I dendritic cells potentiates antitumor immunity. Sci Immunol. 2024. https://doi.org/10.1126/sciimmunol.adj3945.
55. Zhao B, Du F, Xu P, Shu C, Sankaran B, Bell SL, Liu M, Lei Y, Gao X, Fu X. A conserved PLPLRT/SD motif of STING mediates the recruitment and activation of TBK1. Nature. 2019;569(7758):718–22.
56. Imler J-L, Cai H, Meignin C, Martins N. Evolutionary immunology to explore original antiviral strategies. Philos Trans R Soc Lond B Biol Sci. 2024;379(1901):20230068.
57. Zhu J, Fang P, Wang C, Gu M, Pan B, Guo W, Yang X, Wang B. The immunomodulatory activity of lenvatinib prompts the survival of patients with advanced hepatocellular carcinoma. Cancer Med. 2021;10(22):7977–87.
58. Wang D, Qiu G, Zhu X, Wang Q, Zhu C, Fang C, Liu J, Zhang K, Liu Y. Macrophage-inherited exosome excise tumor immunosuppression to expedite immune-activated ferroptosis. J Immunother Cancer. 2023. https://doi.org/10.1136/jitc-2022-006516.

Publisher's Note